Reactive force field potential for carbon deposition on silicon surfaces

2012 J. Phys.: Condens. Matter 24 395004

(http://iopscience.iop.org/0953-8984/24/39/395004)

J. Phys.: Condens. Matter **24** (2012) 395004 (13pp) doi:10.1088/0953-8984/24/39/395004

Reactive force field potential for carbon deposition on silicon surfaces

Ludovic G V Briquet[1], Arindam Jana[1], Lotta Mether[2], Kai Nordlund[2], Gérard Henrion[3], Patrick Philipp[1] and Tom Wirtz[1]

[1] Department 'Science and Analysis of Materials' (SAM), Centre de Recherche Public—Gabriel Lippmann, 41 rue du Brill, L-4422 Belvaux, Luxembourg
[2] Department of Physics, University of Helsinki, FI-00014 Helsinki, Finland
[3] Institut Jean Lamour, UMR CNRS—Université de Lorraine, Department 'Chemistry and Physics of Solids and Surfaces', Ecole des Mines—Parc de Saurupt, F-54042 Nancy, France

E-mail: philipp@lippmann.lu

Received 1 June 2012, in final form 6 July 2012
Published 23 August 2012
Online at stacks.iop.org/JPhysCM/24/395004

Abstract

In this paper a new interatomic potential based on the Kieffer force field and designed to perform molecular dynamics (MD) simulations of carbon deposition on silicon surfaces is implemented. This potential is a third-order reactive force field that includes a dynamic charge transfer and allows for the formation and breaking of bonds. The parameters for Si–C and C–C interactions are optimized using a genetic algorithm. The quality of the potential is tested on its ability to model silicon carbide and diamond physical properties as well as the formation energies of point defects. Furthermore, MD simulations of carbon deposition on reconstructed (100) silicon surfaces are carried out and compared to similar simulations using a Tersoff-like bond order potential. Simulations with both potentials produce similar results showing the ability to extend the use of the Kieffer potential to deposition studies.

The investigation reveals the presence of a channelling effect when depositing the carbon at 45° incidence angle. This effect is due to channels running in directions symmetrically equivalent to the (110) direction. The channelling is observed to a lesser extent for carbon atoms with 30° and 60° incidence angles relative to the surface normal. On a pristine silicon surface, sticking coefficients were found to vary between 100 and 73%, depending on deposition conditions.

(Some figures may appear in colour only in the online journal)

1. Introduction

Interest in plasma surface treatments has become more and more pressing due to their efficient and non-polluting use in surface etching, thin layer deposition or surface functionalization. In order to thoroughly master plasma surface treatment techniques, the understanding of the plasma–surface interactions as well as the understanding of the early stage growth is of prime importance. In this context, molecular dynamics (MD) simulations are currently proving themselves to be a valuable tool for a qualitative description on these two points [1].

Another area of interest including similar problems to the ones encountered in plasma surface treatments, in particular sticking mechanisms in the sub-monolayer regime, is the storing matter technique recently developed at the Centre de Recherche Public—Gabriel Lippmann [2, 3]. This is a new analytical technique where the sample sputtering is decoupled from the subsequent secondary ion mass spectrometry (SIMS) analysis step. Although SIMS analyses are highly sensitive to trace elements, the method is known to have rather poor absolute quantification capabilities because the ionization probability of sputtered particles is strongly dependent on the sample's chemical composition. This so called matrix effect can somewhat be overcome by the use and analysis of standards, i.e. trace elements at a known concentration and in the same chemical matrix as the sample, but it is not always an easy or even possible task, depending on the

sample nature. Instead, by collecting the sputtered sample in the sub-monolayer regime on a known material called a collector, the storing matter technique offers a new strategy to control the matrix effect: the ionization probability depends only on the collector composition, which makes quantification in SIMS much easier. It is also worth noting that the storing matter technique can be used on both organic [4] and inorganic materials [5].

Since the storing matter technique involves the sputtering of an unknown sample followed by its deposition on a collector, it is important, if one wants to preserve the sensitivity of the SIMS analysis, to collect as much material as possible on the collector. It is therefore obvious that, as for plasma deposition techniques, high sticking coefficients are desirable during the deposition of atoms and/or clusters on a known material. The sticking coefficient issue is brought to an entire upper level when using the storing matter technique to analyse samples containing two species or more, as the stoichiometry should be conserved during the sputtering/deposition step as much as possible. The safest way to keep a consistent stoichiometry on the unknown sample and on the collector is to have full control of the sticking coefficients for all species.

The sticking coefficient is highly dependent on the incoming particle (nature, incidence angle, energy) and on the collector (nature, surface relief, crystallinity). It is of prime importance to deepen our knowledge of deposition of atoms/clusters processes in order to identify, for a specific deposition species on a specific collector material, the best conditions to have sticking coefficients as high as possible.

As already stated in the first paragraph of this paper, MD simulations represent a valuable tool for the study of plasma–surface interactions as well as of ion deposition processes [1]. When dealing with low-energy impacts, MD methods are much more suitable simulation tools than binary collision methods [6] as they provide a fully deterministic description of the system of interest over short periods of time [7, 8]. All the interactions between the atoms being deposited and the neighbouring atoms during the cascade collision are thoroughly taken into consideration, which is crucial when the projectiles have a low enough velocity to feel their surrounding chemical environment. The down side of MD methods is the relatively short timescales being handled, normally limited to the nanosecond scale for the longest simulations. This limitation can be overcome by using kinetic Monte Carlo methods, but at the expense of tedious descriptions and hence parameterizations of all events that might happen [9].

We therefore consider MD simulations to be very well suited to understand the deposition process of sputtered particles on a collector within the storing matter scheme. Firstly, the deposition process on the collector is executed at low energy (not exceeding 50 eV). This means the force field potential does not have to deal with situations too far from the equilibrium state and high-energy specialized force fields such as the ZBL repulsive force field [10] are not needed [11, 12]. Secondly, the deposition is done at the sub-monolayer level, with a very diluted deposit on the collector matrix. As a consequence, the amorphization of the collector is limited and single impacts on a pristine crystalline surface can be used as a first approximation to model the first stages of the deposition.

This study presents the very first steps towards the simulation of storing matter analyses of alloy materials such as WC, TiC, or TiCN, using silicon wafers as collector. Within this framework, the carbon–silicon interactions play a central role and we use MD simulations with the reactive force field developed by John Kieffer and co-workers [13–16] to gain a better understanding of the interactions between carbon and silicon surfaces. Kieffer's force field is newly developed and allows for the possibility to account for the breaking and formation of bonds as well as for a dynamic charge transfer between pairs of atoms. A Kieffer force field parameter set is available in the literature for Si–Si interactions [16, 17], but is missing for Si–C and C–C interactions. The first part of this paper therefore presents a newly derived parameter set for the C–C and C–Si interactions, suitable for Kieffer's force field. The new force field is tested on its abilities to model several physical properties of diamond and silicon carbide, as well as to compute the formation energy of several point defects in these structures. In order to further check the suitability of our potential for carbon interaction with silicon surfaces, we present in the second part of this paper a comparison of low-energy carbon deposition (from 1 to 50 eV) at various incidence angles on a Si(100) surface using our new Kieffer potential sets and the well-established Erhart–Albe potential [18]. In addition, a comparison with carbon adsorption sites as computed using DFT methods is also presented.

2. Computational details

2.1. Kieffer interatomic potential

The reactive force field developed by Kieffer and his co-workers [13–16] has been used throughout this paper. This force field has been specially built to allow the formation and breaking of bonds in the system via an adaptable and environment sensitive charge transfer routine and via an angular term that dynamically adapts itself to the valence of the atoms. The analytical form of the force field includes a Coulomb term, a Born–Huggins–Mayer repulsive term and a three-body term:

$$\phi_i = q_i \sum_{j=1}^{N} \frac{q_j}{4\pi\varepsilon_0 r_{ij}} + \sum_{j=1}^{NC} C_{ij} \mathrm{e}^{(\sigma_i+\sigma_j-r_{ij})\cdot\rho_{ij}} + \sum_{j=1}^{NC-1} \sum_{k=j+1}^{NC} (\varphi_{ij}+\varphi_{ik})(m \cdot \mathrm{e}^{-\gamma_{ijk}(\overline{\theta}-\theta_{ijk})^n} - (m-1)). \quad (1)$$

Within this framework, q_i represents the charge of the particle, ε_0 is the dielectric constant of the vacuum, and r_{ij} is the interatomic distance. The charge transfer term allows for the atomic charge to be modified following $q_i = q_i^0 - \sum_{j=1}^{NC} \delta_{ij}\zeta_{ij}$, where q_i^0 is the charge of the isolated atom, δ_{ij} is the amount of charge that can be transferred between two atoms,

and $\zeta_{ij} = \frac{1}{1+e^{b(r_{ij}-a)}}$ is the charge transfer function (a and b are empirical parameters). Covalent bonding is modelled by $(\varphi_{ij} + \varphi_{ik})(m \cdot e^{-\gamma_{ijk}(\bar{\theta}-\theta_{ijk})^n} - (m-1))$, where $\varphi_{ij} = -C_{ij}\frac{\kappa_{ij}}{\eta_{ij}}\zeta_{ij}e^{(\lambda_{ij}-r_{ij})\eta_{ij}}$, $\bar{\theta}$ is the equilibrium bond angle, θ_{ijk} is the angle formed by the bond vectors r_{ij} and r_{ik}, and m is a parameter enabling repulsive forces at bond angles far from equilibrium. Furthermore, $C_{ij} = A_{ij}(1 + \frac{z_i}{n_i} + \frac{z_j}{n_j})$, where z_i is the valence and n_i is the number of electrons in the outer shell of atom i. A more detailed discussion of the force field can be found in [16] and references therein.

The parameter set describing the Si–Si interaction is available in the literature [16, 17]. The parameter sets for C–C and Si–C interactions will be presented in the next paragraphs.

2.2. Erhart–Albe interatomic potential

The interatomic potential by Erhart and Albe [18] is a Tersoff-type analytical bond order potential [19] for Si–C systems. The potential is short-ranged and accounts only for nearest-neighbour interactions by employing a cutoff function, which drops the atomic interaction to zero in between the first and second nearest-neighbour distance. In this paper, the potential has been utilized with the Si–I parameter set for MD simulations of carbon deposition on a (100) silicon surface to compare with the Kieffer potential results.

2.3. Genetic algorithm for parameter sets generations

For the generation of C–C and C–Si parameter sets within the Kieffer potential framework, a similar methodology to the one used in [17] for the Si–Si parameter set generation has been used. By combining MD simulations to a genetic algorithm, a large number of parameters sets are evaluated and optimized until a set with the desired accuracy is found. For each individual (i.e. each trial parameter set) in the genetic algorithm population, MD simulations in the isothermal–isobaric (*NPT*) ensemble at 300 K on the experimental bulk crystalline structure representing the atomic pairs of interest are run and the simulated physical parameters are compared to their experimental values. According to their ability to match experimental data, each individual is scored and a ranking table is built. Individuals in the bottom half of the table (poorest ranking) are replaced by new individuals. Parameters from the top half individuals are mixed to create the new individuals, mimicking the evolution of a population following Darwin's law, where only the fittest individuals get the chance to give part of their 'genes' to the next generation. A pre-evaluation test is performed each time a new individual is created. This pre-evaluation test consists in ensuring that the parameter sets give a correct bond length and bond energy for the bond corresponding to the atom pair being fitted. For the evaluation process, performed after the MD runs, the fitness of each individual is evaluated by comparing the density, the radial distribution function, the phonon vibration frequencies and the elastic constants of its crystalline structure.

- The density is calculated by averaging the simulated density over the last 10 ps of the MD simulation, which allows us to avoid interference due to the initial relaxation of the unit cell. The value is then simply matched against the experimental density.
- The evaluation of the radial distribution is done by localizing the position of the first peak, corresponding to the bond length of interest. The score is defined as the percentage of the difference between the bond length derived from the experimental unit cell size and the position of the first peak on the radial distribution function graph.
- The phonon vibration frequencies are evaluated by analysing the position of a number of peaks in the phonon density of state spectrum. The position of the first peak has to be within some range corresponding to the experimental value of the vibration frequencies. A stability factor has been added to the phonon density curve evaluation in order to penalize very chaotic curves containing many small peaks.
- To compute the elastic constants eight additional MD runs are necessary. The three independent elastic constants, C_{11}, C_{12}, C_{44}, are evaluated by measuring the evolution of the internal stress tensor versus strain on the lattice. For C_{11} and C_{12}, the equilibrated lattice constants are incrementally increased by 1% in the [100] direction. Four MD runs in the NVT ensemble are performed and the outputted stress components σ_{11} and σ_{22} are plotted against the strain ε_{11}. Linear regression evaluation by the least square method is then performed to estimate the slope of the line, which is C_{11} for σ_{11} and C_{12} for σ_{22}. C_{44} is evaluated using the same methodology but by following σ_{23} against the strain ε_{23}. The computed values for C_{11}, C_{12}, and C_{44} are then compared to their experimental values.

2.4. DFT calculations

All first principles calculations are performed with the SIESTA DFT package [20] using the Perdew–Burke–Ernzerhof gradient approximation (GGA-PBE) [21]. A Troullier–Martins pseudo-potential is used for the representation of carbon and silicon ionic cores [22]. The basis set is DZP as described in [23]. A k-point mesh of $2 \times 2 \times 1$ and a mesh cutoff of 150 Ryd are used for the $2 \times 2 \times 4$ surface supercell. The slabs are separated by a 38 Å vacuum gap. The self-consistent cycles are performed until an energy threshold of 10^{-4} eV is met. Force and displacement thresholds for the conjugate gradient geometry optimization procedure were set to 0.04 eV $Å^{-1}$ and 0.026 Å, respectively.

3. Carbon–carbon parameter set

The parameter set for the C–C interactions within the Kieffer force field framework is determined using the genetic algorithm, as described in [17]. The pre-evaluation phase for each generated parameter set checks that the bond energy is within 5% of 7.37 eV [24] and that the bond length is within

Table 1. Physical properties for diamond and silicon carbide as reported in the literature and as computed using the C–C and SiC parameter sets for the Kieffer force field.

Diamond		Literature		This work
Density (g cm^{-3})		3.51[a]		3.51
C–C bond length (Å)		1.54[b]		1.54
C_{11} (GPa)	1075[c]		1082[a]	1151
C_{12} (GPa)	125[c]		127[a]	231
C_{44} (GPa)	577[c]		635[a]	481
Phonon frequencies (cm^{-1})		552[d]		See figure 1
		803[d]		
		1035[d]		
		1200–1300[d]		
		1331[d]		
Silicon carbide				
Density (g cm^{-3})		3.21[e]		3.21
C–C bond length (Å)		1.88[f]		1.88
C_{11} (GPa)	390[f]	382[a]	254[g]	357
C_{12} (GPa)	142[f]	145[a]	225[g]	100
C_{44} (GPa)	256[f]	240[a]	66[g]	143
Phonon frequencies (cm^{-1})		310[h]		See figure 2
		550[h]		
		750[h]		
		850[h]		

[a] MD—Erhart [18].
[b] DFT + Exp: [25].
[c] Exp. [26].
[d] Exp. [27].
[e] Exp. [28].
[f] DFT + Exp. [29].
[g] MD—Gao [30].
[h] DFT [31].

5% of 1.54 Å [25]. MD simulations for each parameter set are run using a 3.567 Å wide diamond unit cell as starting point; the simulation time step is 1 fs and the total simulation time length is 200 ps. The individual evaluation phase assesses each parameter set according to its ability to reproduce the diamond density, C–C bond length, elastic constants, and phonon density of state, as reported in table 1. It should be noted that the diamond phonon density of state presents a very broad band from 400 to 1400 cm^{-1} [27], containing several more or less marked peaks that are reported in table 1.

The generated Kieffer C–C parameter set, presented in table 2, performs very well in modelling the density and the C–C bond length as measured by the radial distribution function. Other physical properties such as the elastic constants and the phonon vibrations are on the other hand more complex to reproduce as they involve the internal stress of the crystal. Thus, in order to favour a greater transferability of the potentials (SiC parameters, ...), we have decided to allow the simulated physical properties to diverge a little from their experimental value at the condition of meeting a better general agreement between all screened physical properties. Although the C_{12} elastic constant is not perfectly reproduced, C_{11} and C_{44} are well modelled. The simulated phonon density of state spectrum computed on an 8 × 8 × 8 supercell is presented in figure 1. In agreement with the literature, the phonon spectrum is a broad band ranging from 400 to

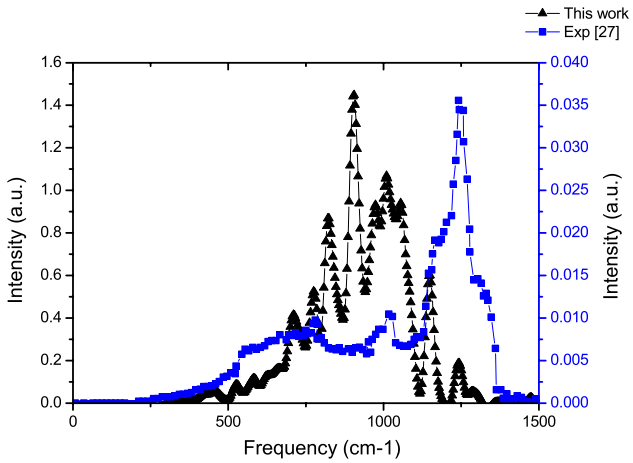

Figure 1. Comparison between the computed phonon density of states of diamond using Kieffer potential and the experimental data [27].

1300 cm^{-1}. The peak that was reported in the literature at 1035 cm^{-1} [27] appears in our calculation at 900 cm^{-1}. The vibration frequencies reported at 1200 and 1331 cm^{-1} [27] are also underestimated in our simulation, as they appear at 1000 and 1100 cm^{-1}. On the overall, the agreement with the literature data is moderate, as the most intense bands are shifted towards lower frequencies.

Table 2. Parameters for the Si–Si and Si–C interactions.

Element		σ_i (nm)	n_i	z_i	q_i^0
Si		0.101	8	+4	0
C		0.095	8	+4	0
Pair	A_{ij} (10^{-19} J)	ρ_{ij} (nm^{-1})	λ_{ij} (nm)	η_{ij} (nm^{-1})	κ_{ij} (nm^{-1})
Si–Si	1.80	91.00	−1.31	2.00	91.00
Si–C	0.38	39.22	−10.99	0.22	36.59
C–C	0.012	87.22	1.24	1.79	140.31
Charge transfer		δ_{ij} (e)	a (nm)	b (nm^{-1})	
Si–Si		0.000	0.293	110.0	
Si–C		0.095	0.243	47.89	
C–C		0.000	0.199	85.61	
Triplet		γ_{ijk} (rad^{-n})	θ (rad)	n	m
Si–Si–Si		4.60	1.91	4	4
Si–C–Si		1.20	1.91	2	1
C–Si–C		0.55	1.91	2	1

As a further check for the Kieffer C–C interatomic potential, the formation energies of several point defects in the diamond structure are also computed and compared to the literature data (table 3). A 5 × 5 × 5 unit cell is used to compute the defect formation energies. Among the possible defects reported, the vacancy (V) and three types of interstitial defects (I_T for the tetrahedrally coordinated, I_S for the ⟨100⟩ split, and I_B for the bond-centred interstitial atom) are chosen for this comparison. There is an excellent agreement between our computed vacancy formation energy (7.40 eV) and the ones reported in DFT investigations (7.51 and 7.20 eV [32, 33]). It should also be noted that the Erhart–Albe potential predicts a formation energy of 5.24 eV [18], lower than the DFT values. DFT investigations predict that interstitial defects are significantly less favourable than vacancies [32]: with 15.8 and 16.7 eV, I_B and I_S have similar defect formation energies, while, with 23.6 eV, I_T has a much higher formation energy. The Erhart–Albe potential predicts formation energies for I_T and I_B, in line with DFT (23.90 eV and 16.06 eV, respectively), but, with 10.21 eV, I_S is predicted to be significantly favoured over other interstitial defects [18]. Although computed formation energies using the Kieffer potential are lower than the DFT values, we obtain a better quantitative agreement than Erhart *et al* [18]. Formation energies of I_B (8.23 eV) and I_T (8.60 eV) are predicted to be similar and to be higher than the vacancy (7.40 eV). The formation energy of I_T (15.32 eV) is predicted to be much higher than any other defects.

Table 3. Formation energies (eV) of point defects in diamond and silicon carbide. Within diamond point defects, V stands for vacancies; I_T, for tetrahedral interstitial; I_S for ⟨100⟩ split interstitial; I_B, for bond-centred interstitial. Within the silicon carbide point defects, V_X stands for a vacancy of specie X; X_Y, for substitution of lattice specie Y by specie X; X_{TY}, for tetrahedral interstitial X surrounded by four species Y; X_{SY}, for a specie X ⟨100⟩ split interstitial near a specie Y.

Defect	Formation energies (eV)					
	DFT		MD			
C	[32]	[33]	[18]	This work		
V	7.2	7.51	5.24	7.40		
I_T	23.6	23.65	23.90	15.32		
I_S	16.7		10.21	8.60		
I_B	15.8		16.06	8.23		
	DFT			MD		
SiC	[34]	[18]	[18]	[18]	[30]	This work
V_C	5.48	5.11	4.5	1.90	2.76	6.36
V_{Si}	6.64	8.01	8.2	4.55	3.30	8.47
C_{Si}	1.32	4.06	3.8	2.42	1.69	18.51
Si_C	7.20	4.46	4.6	2.48	7.79	11.08
C_{TC}	6.41	7.78	12.4	12.63	4.65	7.71
C_{TSi}	5.84	7.21	10.0	9.38	4.32	12.10
Si_{TC}	6.17	4.80	13.3	17.55	3.97	8.71
Si_{TSi}	8.71	7.34	13.6	17.30	6.77	8.81
C_{SC}	3.16	4.53		4.78	3.04	10.62
C_{SSi}	3.59	4.49		8.31	3.43	9.49
Si_{SC}	10.05	8.68		14.14	7.54	7.22
Si_{SSi}	9.32	7.95		20.90	5.53	12.20

4. Silicon–carbon interactions

As for the C–C interactions, a genetic algorithm [17] is used to determine the Si–C parameter set. The pre-evaluation phase for each parameter set generated by the genetic algorithm checks that the bond energy is within 5% of 6.4 eV [29] and that the bond length is within 5% of 1.88 Å [29]. MD simulations for each parameter set are run using a 4.359 Å wide 3-C silicon carbide (zinc-blende structure) unit cell as starting point; the simulation time step is 0.5 fs and the total simulation time length is 50 ps. The parameter controlling the amount of charge transfer is determined to reflect the Mulliken atomic charges computed in silicon carbide by DFT (0.76e). The individual evaluation phase assesses each parameter set according to its ability to reproduce the silicon carbide density, Si–C bond length, elastic constants, and phonon density of state as reported in table 1. It should be

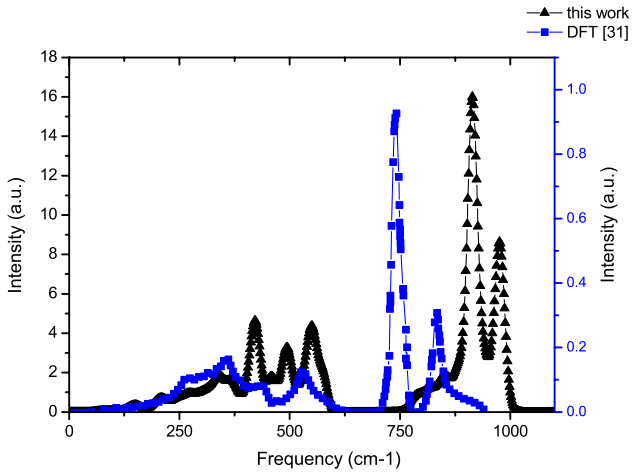

Figure 2. Comparison between the computed phonon density of states of silicon carbide using the Kieffer potential and the DFT data reported in [31].

noted that the silicon carbide phonon density of state presents a couple of broad bands from 250 to 450 cm^{-1} and from 500 to 650 cm^{-1}. In addition to these low frequency broad bands two sharper bands are located at 750 and 850 cm^{-1} [31].

As for the C–C parameters, the Kieffer C–Si parameter set, presented in table 2, performs very well in modelling the density (3.21 g cm^{-3}) and the C–Si bond length (1.88 Å) as measured from the radial distribution function. Phonon vibration frequencies and elastic constants are much more difficult to reproduce exactly with a single transferable potential. Therefore, as for the C–C parameters, we allow an error margin for those physical properties instead of focusing on modelling exactly one property regardless of the other ones. The simulated elastic constants are 357 and 100 GPa, for C_{11} and C_{12} in good agreement with experimental data. With 143 GPa, the C_{44} elastic constant deviates more from the experimental value. The simulated phonon vibrations computed using an $8\times8\times8$ supercell and presented in figure 2 show a main large band centred between 200 and 600 cm^{-1}, comprising several peaks matching the experimental vibration frequencies 310 and 550 cm^{-1}. At higher frequencies two sharp peaks can be observed. The first peak at 900 cm^{-1} corresponds to the reported peak 750 cm^{-1}, while the second at 1000 cm^{-1} corresponds to the peak at 850 cm^{-1} in the literature [31]. There are indeed some quantitative deviations from our simulated vibration frequencies and elastic constants compared to the experimental values. It is, however, known that if one focuses the parameterization of a force field parameter set to fit perfectly one physical property, large deviations may be expected in the description of other physical properties. For example the Gao Si–C parameter set [30] was designed to reproduce defect energies from plane wave DFT calculations [34], but, although this potential reproduces nicely the DFT results (table 3), it has been shown to perform poorly when computing silicon carbide elastic constants [18] (table 1).

In order to verify further the transferability of our Kieffer potential, the energies of several point defects in silicon carbide have been computed and compared to literature data. Among the possible defects in silicon carbide, the two types of vacancies (V_c and V_{Si}), the two antisite defects (C_{Si} and Si_C) and eight interstitial defects where the interstitial atom is tetrahedrally coordinated by four C or Si atoms (C_{TSi}, C_{TC}, Si_{TC}, and Si_{TSi}) and where the interstitial atom is in a ⟨100⟩ split position (C_{SSi}, C_{SC}, Si_{SC}, and Si_{SSi}) have been considered. Defect formation energies are computed using a $5\times5\times5$ unit cell, following the methodology proposed by Nord *et al* [35]. Results are presented in table 3. From the literature, one can see that, unlike for diamond, there are rather large discrepancies in the defect formation energies computed with DFT methods [18, 34]. It should also be noted that as the potential developed by Gao *et al* [30] focuses on modelling point defects, there is a relatively good overall agreement with DFT results in [34]. The Erhart–Albe interatomic potential, on the other hand, seems to be less able to match DFT data for interstitial defects, even though it performs very well for other silicon carbide physical properties [18]. The Kieffer potential performs very well for both types of vacancies as they are better reproduced with our potential than with others: carbon and silicon vacancies are predicted to be 6.36 and 8.47 eV, in very good agreement with the DFT values reported in [18] (5.11 eV and 8.01 eV, for carbon and silicon respectively), while Gao's potential, which was specifically designed to model point defects, gives lower formation energies of 2.76 and 3.30 eV. Some discrepancies start to appear when considering antisites and interstitial defects. Based on the different trends obtained by DFT methods, it is, however, difficult to precisely assess the quality of our potential. The Kieffer potential overestimates the formation energy of the C_{Si} defect, as it predicts a formation energy of 18.51 eV, while all other methods report values ranging from 1.62 to 4.06 eV [34, 18]. This discrepancy probably originates from an overestimation of the Si–C bond energies at distances longer than the equilibrium bond length. On the other hand, the Kieffer potential is in relatively good agreement with the literature for the formation energies of silicon interstitial ⟨100⟩ split. It predicts energies of 7.22 eV and 12.20 eV for Si_{SC} and Si_{SSi}, respectively, while DFT predicts 8.68 and 7.95 eV [18]. The performance of our potential on this type of point defect is better than the Erhart–Albe potential, as the latter largely overestimates ⟨100⟩ split interstitials (14.14 eV and 20.90 eV for Si_{SC} and Si_{SSi} respectively). Despite these deviations, when comparing the formation energies of interstitial defects, the Kieffer interatomic potential generally stands within the same range of performance as the ones computed with the Erhart–Albe or the Gao potentials.

As we are dealing with impact processes, and although the energies considered are low, it is expedient to check how the repulsive part of the C–Si potential is reproduced as compared to the Erhart–Albe potential [18] and to in-house calculation using DFT methods (figure 3). Within the energy range of interest for this study (i.e. lower than 50 eV) only small energy differences can be seen between Erhart–Albe's and our potential. The differences in energy start to be more noticeable at energies higher than 50 eV. When increasing the energy, repulsive forces become in general steeper

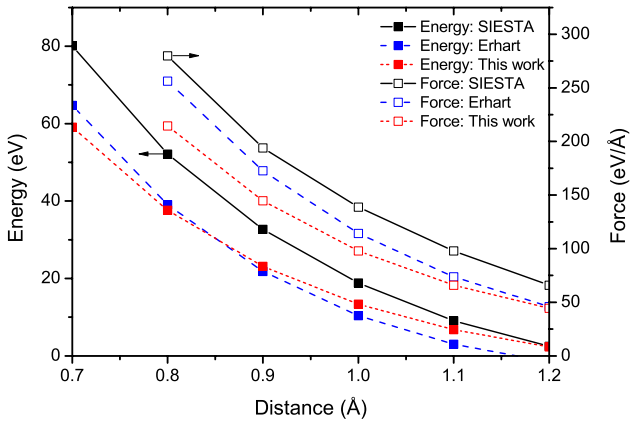

Figure 3. Comparison of evolutions of potential energies and forces at short distances for Kieffer and Erhart–Albe potentials and for DFT.

with the Erhart–Albe potential than Kieffer's one. They, however, remain within the same range at low energies. Both interatomic potentials show a reasonable agreement with DFT data, albeit with slightly lower energies and forces.

5. Carbon deposition

5.1. Computational settings

The new Si–C parameter set is used to investigate carbon deposition processes on crystalline (100) silicon surfaces. In order to double check the results generated with Kieffer's force field and to validate the Si–C potential for the specific application of carbon deposition on silicon surfaces, MD simulations of carbon deposition using the Erhart–Albe potential [18] are also carried out for selected energies and incidence angles.

Within the Kieffer force field framework, the simulation cell is a fixed 8 × 8 × 8 supercell containing 4096 Si atoms. Periodic boundary conditions are applied in the three directions of space and a 17 nm vacuum gap in the z direction is applied to separate the silicon surface from its image. The surface is relaxed during 100 ps, resulting in the formation of silicon dimers on the surface. There is some randomness at the surface and the dimers are not all perfectly aligned. A carbon atom is then added randomly at a fixed distance above the surface with a defined downward velocity. Velocities are determined as to correspond to energies of 1, 3, 5, 7, 9, 10, 20, 30, 40, or 50 eV at 0°, 15°, 30°, 45° and 60° incidence angles (angles defined with respect to the surface normal, also called elevation angles). The azimuth angles, which, together with the incident angle, define the initial directions of the carbon atom, are randomly set for each simulation. For each impact energy and incidence angle, 100 independent simulations (i.e. each simulation corresponds to one C impacting on a pristine surface) are performed in order to have meaningful statistics. The incoming carbon atom bears no charge, since adding a charged particle would alter the neutrality of the simulation box, resulting, with the periodic boundary conditions, in a system having an unphysical infinite charge. The MD time step is set to 0.2 fs for a total simulation length of 6 ps. This short timescale is enough for the system to dissipate the impact energy, considering that it does not exceed 50 eV. No energy control was applied in the simulations.

Within the Erhart–Albe potential framework, the simulation supercell is 8 Si lattice constants thick with a reconstructed (100) surface of 12 rows of 6 perfectly aligned dimers, consisting of 4608 Si atoms in total. As with the Kieffer potential, a carbon atom is placed randomly at a fixed distance above the surface, and deposited with a definite velocity and angle of incidence; in this case, velocities corresponding to energies of 1, 3, 10, 30 and 50 eV and incidence angles of 0°, 30° and 60° are considered. For each combination of energy and incidence angle, the simulation is independently repeated 300 times, with different random starting point and azimuth angle for the carbon atom. Before deposition, the silicon lattice has been equilibrated at a temperature of 300 K, using the Berendsen thermostat [36] with a time constant of 20 fs. The thermostatting is only performed at the boundaries. A relatively short value of 20 fs has been found to be good for efficient damping of most of the heat wave emanating from the collision cascades. On the other hand, we have previously shown that the results of cascade calculations are not sensitive to the boundary cooling time constant [37]. The carbon depositions are simulated with a maximum time step of 1.8 fs for a total time of 5 ps. The difference in the time step between the Kieffer and Erhart–Albe potentials is explained by the use of a constant time step for the former and a variable time step [38] for the latter set of simulations.

5.2. Results

5.2.1. Backscattering of carbon atoms. The proportions of carbon being implanted, deposited and backscattered are computed using both Kieffer and Erhart–Albe interatomic potentials at selected impact energies and angles. A carbon atom is considered as being implanted after impact with the silicon surface if its position at the end of the MD simulation is beneath a virtual plane located 0.5 Å below the topmost silicon atom of the surface. Carbon atoms located above that virtual plane at the end of the MD simulation and not reflected by the surface are considered as being deposited. Blue lines in figure 4 show the backscattering yields for carbon deposition on a flat surface at different deposition angles and energies. For incidence angles of 0°, 15°, and 30°, a backscattering yield lower than 11% is always observed. Increasing the incidence angle to 45° and 60° will gradually lead to a significant direct loss of matter at higher energies via backscattering of the incoming particle upon impact with the silicon surface. Using the Kieffer potentials and with an incidence angle of 0°, the backscattering yield stands between 0% and 8%, while it is in the range 0–5%, 0–7%, 0–14%, and 0–27% for 15°, 30°, 45°, and 60°, respectively. The backscattering yields for 0° and 30° are very close to the ones computed with the Erhart–Albe potential, as the observed range with this potential is 0–5% for 0° and 2–11% for 30°. At

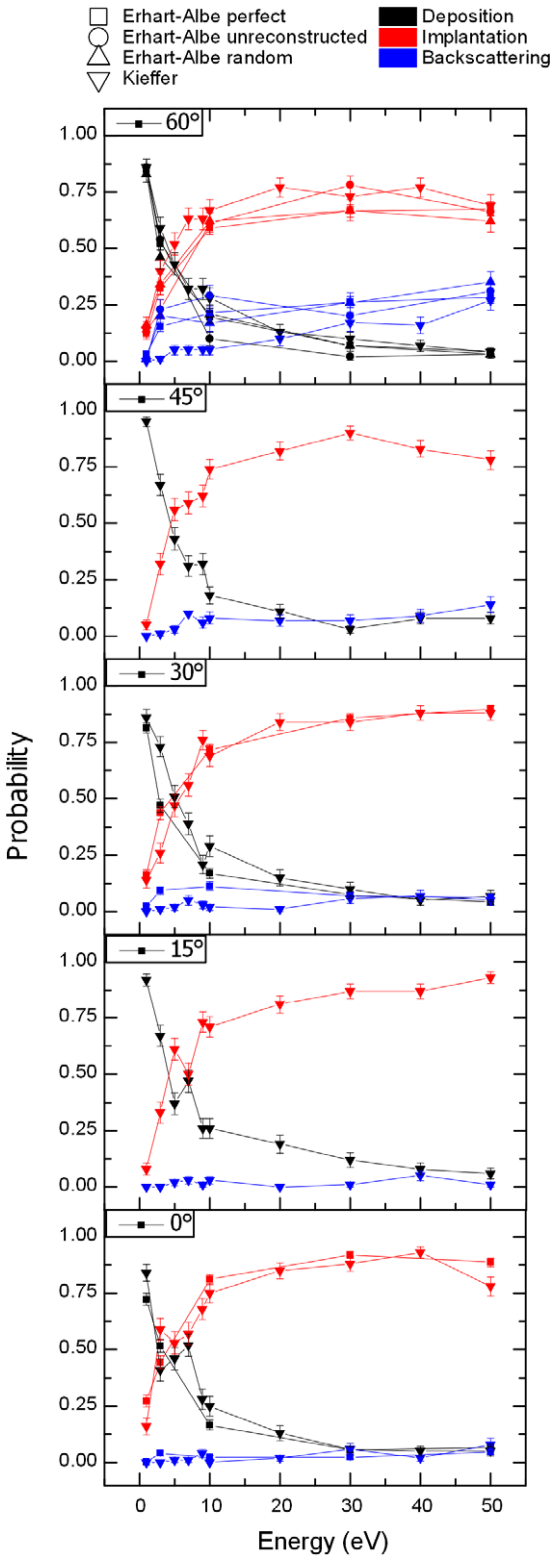

Figure 4. Ratios between deposition (black), implantation (red) and backscattering (blue). Deposition is defined as a carbon atom on top of the silicon surface, while implantation means a carbon atom beneath the silicon surface plane.

60°, the agreement between the two potentials is not as good since the Erhart–Albe potential predicts higher backscattering yields at low deposition energies. This little discrepancy between the potentials at 60° can also, albeit to a lesser extent, be observed in the deposition and implantation yields. Here it should be recalled that there is a small difference in the reconstruction of the silicon surfaces with the Kieffer potential (presence of randomness) and with the Erhart–Albe potential (dimers aligned). Tests using a non-reconstructed (100) surface and the randomly reconstructed (100) surface with the Erhart–Albe potential at 60° incidence angle enables us to rule out an effect of the surface relaxation on the deposition and backscattering rates. We presume that the slight discrepancy at 60° is due to the fact that the two force fields use very different approaches and hence the forces acting between atoms may be different. From figure 3, it is seen that the Erhart–Albe potential allows Si–C bonds to be shorter at low energies but with slightly steeper repulsive forces, which increases the probability for backscattering at grazing angles.

5.2.2. Implantation of the carbon. Next, we address the issue of whether the carbon deposits above the surface, or goes beneath the first silicon plane of the surface. To answer this question, figure 4 presents for each impact angle the proportion of carbon atoms that stay on the surface (deposited—black lines) or go deeper into the material (implanted—red lines). As could be expected, the lower the energy, the more likely is deposition compared to implantation. At 1 eV and for all angles, the deposition/implantation ratios are within 83/17 and 95/5 for both potentials, meaning a vast majority of the carbon atoms stay on top of the surface. When increasing the energy of the carbon, the ratio deposition/implantation rapidly drops. Broadly speaking, and for all incidence angles tested with the Kieffer potential, the implantation rate overcomes deposition when the energy of the carbon atom is higher than 5 eV. Increasing the energy to values higher than 20 eV does not have an impact on the deposition/implantation ratios, as most of the carbon atoms are implanted.

In figure 5 the dispersion of deposition depths for selected energies and incidence angles are presented. Figure 6 shows the average depth reached by the carbon projectile for each impact and incidence angle. The depth is computed by taking the difference in z coordinates of the impact point on the substrate and of the final configuration of the carbon atom. Backscattered atoms are ignored whenever averages are computed. Both potentials are presented in figures 5 and 6 and no major methodological effects can be observed. The higher backscattering yields that have been observed in figure 4 for deposition at low energies coupled with a 60° incidence angle have no impact on the depth reached by the carbon. Instead, the largest differences in the implantation depths between the two potentials are observed for the higher deposition energies at 30° and 60° incidence angles. These divergences stay within the error bars and are not systematic, since at 50 eV–60° the Erhart–Albe potential provides a slightly deeper implantation and at 50 eV–30°, it is the Kieffer potential that provides the deepest implantation. From figure 5, it can be seen that the shallower implantation for the Kieffer potential at 50 eV–60° is due to a higher stopping

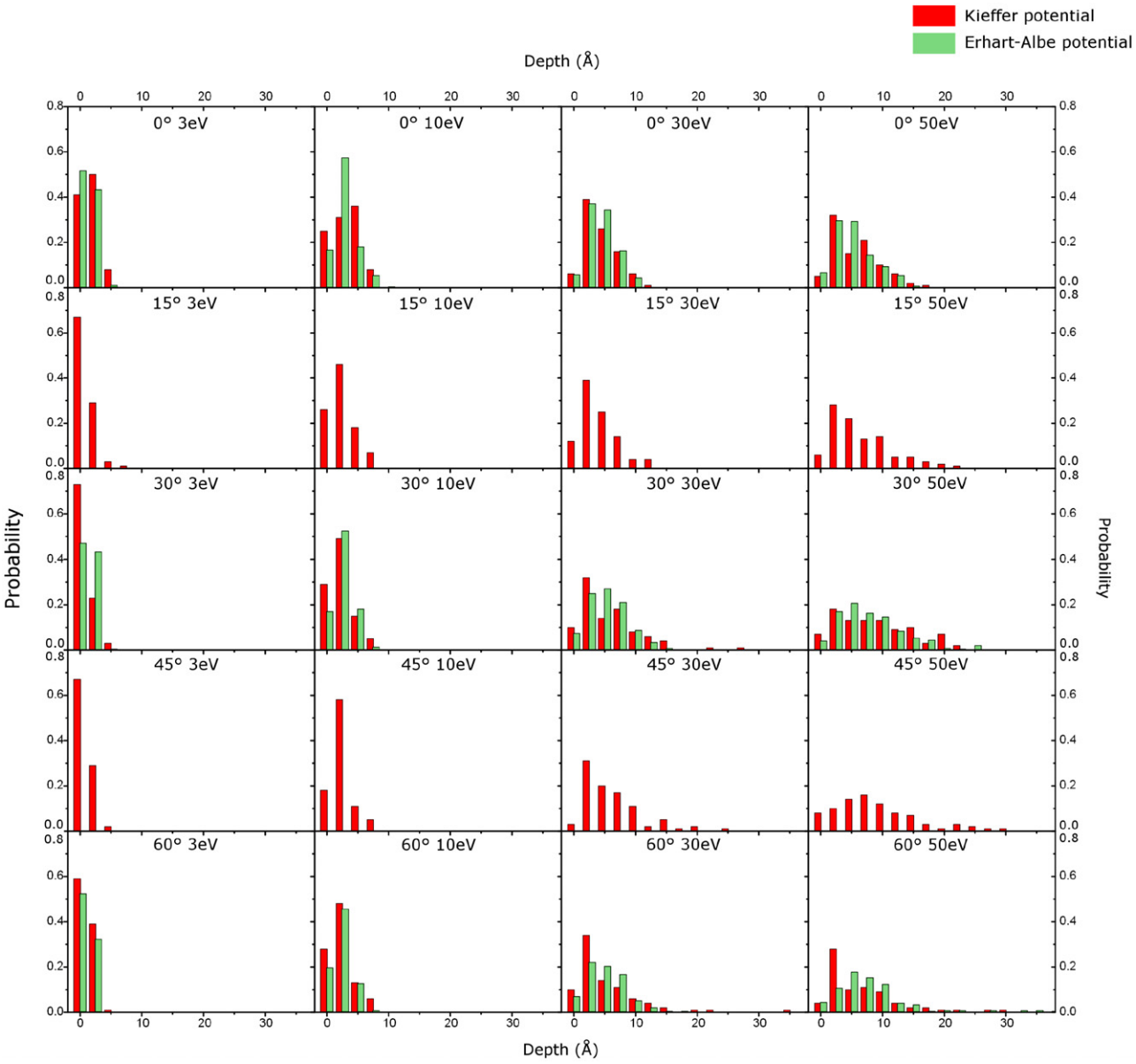

Figure 5. Depth distributions computed with the Kieffer (red) and the Erhart–Albe (green) potentials for selected incidence angles and energies.

power of the material at shallow depths. Similarly, the deeper implantation at 50 eV–30° for the Kieffer potential is due to a tail in the depth distribution extending deeper than for the Erhart–Albe potential. The reasons for these discrepancies will be discussed later in this paper.

At his point of the analysis it is already clear that the limitation of the Kieffer potential to carbon sp^3 hybridization has no dramatic effect on the carbon deposition. Indeed a large part of the carbon effectively goes beneath the surface plane where carbon has the most possibilities to stay in a sp^3 configuration. The Erhart–Albe potential, being of a bond order analytical form, naturally includes the different carbon hybridizations. As seen above, the depth distributions as computed with the two potentials are in fair agreement with each other and the few discrepancies cannot be accounted for the hybridization of the carbon atom.

Looking at figure 6, one can observe that the incidence angle has no influence on the average depth of the deposited carbon at energies up to 20 eV. The dispersion of depths for the lower half of the deposition energies (figure 5) are also very similar when comparing incidence angles at selected energies, confirming the incidence angle does not influence the depth reached by a carbon projectile having a kinetic energy lower than 20 eV. At higher energies, this is no longer true, since incidence angles of 30° and 45° lead to the deepest mean deposition depth and incidence angles of 0° and 15° to the shallowest. The average depths reached by deposition performed at 60° incidence angle lie in between these two extremes. The analysis of the depth dispersion on figure 5 brings some useful insights on the issue. The dispersions of depths at 30 and 50 eV are very similar when comparing simulations at 0° and 15° incidence angles. The most probable

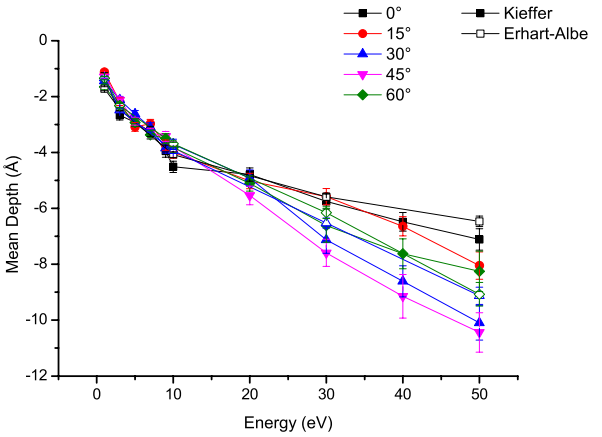

Figure 6. Evolution of the average depth versus the deposition energy as computed using Kieffer and Erhart–Albe potentials. The depths are computed as the differences in the z coordinates of the impact location and the final location of the carbon atom.

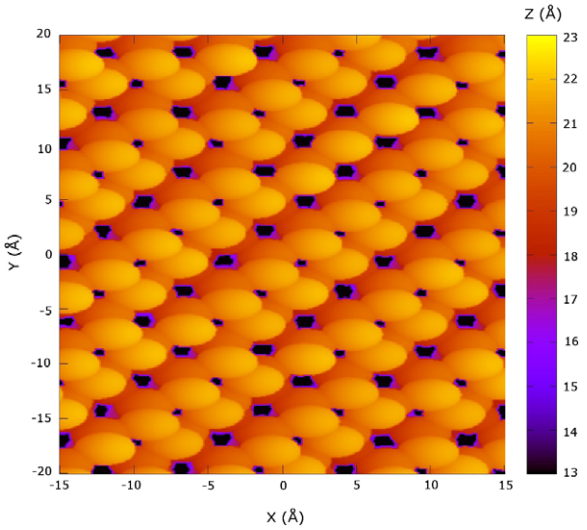

Figure 7. Accessible surface area for a 1.5 Å radius atom having a trajectory at 45° from the (100) Si normal.

depth reached by the carbon is 2.5 Å. The probability to find the carbon atom at a selected depth then gradually decreases when going deeper into the sample. For energies of 30 eV, this probability virtually reaches 0 after a depth of 10 Å for both incidence angles, while at 50 eV this point is reached at 17.5 Å for normal incidence and 20.0 Å for 15° incidence. At incidence angles of 30° and 45°, the situation is completely different. The most probable depth at 30 eV is still located within 2.5–5.0 Å for both incidence angles, but the absolute probability to find a carbon at that depth is lower than the absolute probability observed at normal and 15° incidence. In addition, the tails of the distributions extend much deeper into the sample (down to 15 Å at 30° incidence and to 20 Å at 45°). Looking at the depth distributions for simulations carried out at 50 eV, the difference with the 0°–15° incidence angles is even more flagrant, as the depth distributions for 30° and 45° is nearly flat, with an almost constant probability to find the carbon atom between depth 0 Å and depth 20 Å. In addition, it should be noted that only few carbon atoms were observed far deeper than 20 Å for the 30° and 45° incidences. At the most grazing angle of 60°, the shapes of the depth dispersions computed with the Kieffer potential are between the ones of 0°–15° incidence angle and the ones of 30°–60°. For both 30 and 50 eV energies, the most probable depth is clearly at 2.5 Å but as for the 30°–60° incidence angle simulations, the tail extends very deep inside the silicon bulk and few carbon atoms can be observed at depths much deeper than 20 Å.

Raineri *et al* have reported that when implanting boron and phosphorus in crystalline silicon at several directions, the depth profiles present a single maximum intensity for all directions except the (110), where a second intensity maximum is observed at significantly deeper depths [39]. Similarly, as seen in the previous paragraph, when depositing carbon at angles close to 45° incidence angles, part of the flux is stopped at a shallow depth, while the rest of the flux can reach a deeper part of the silicon sample. The reason for these different behaviours in the dependence of the depth distribution on the incidence angles is attributed to narrow channels running through the bulk structure in the (110) direction and its symmetry-equivalent directions. Part of these channels indeed intersect the (100) surface plane with an angle of 45° relative to the normal of the surface and are available to the carbon projectile. Figure 7 shows the (101) projection of the accessible surface area for an ion size 1.5 Å. The colouring is set depending on the achievable depths and the channels are clearly visible as black dots. As a consequence of this orientation, only the carbons having an incidence angle close to 45° are allowed to enter the channels. Carbon depositing with an incidence angle of 0° and 15° are too far from this 45° optimum and are stopped at very shallow depths. Our simulations also show that incidence angles of 30° and 60° are still within the correct window, to allow the carbon to enter the channels and reach a deeper part of the silicon sample. One can argue that the probability for the carbon to enter the channels depends on the cutoff distance for C–Si bonds within the potentials, especially if they are too short as compared to the channel size. It should however be noted that the cutoff value for short range interactions is set to 3.0 Å for the Kieffer potential and to 2.60 Å for the Erhart–Albe potential, i.e., in all cases larger than the radius of the channels (∼2.25 Å).

As stated in the previous paragraph, there are four equivalent directions to the (110) vector going through the (100) plane, meaning that on an azimuth plane parallel to the surface, four orthonormal channels meet the (100) plane (figure 8). This explains why there is such a wide distribution of achievable depths for 30°, 45°, and 60° incidence angles. Carbon projectiles that do not possess the right azimuth trajectory cannot enter the channel and are stopped at shallow depths, while others will go deeper inside the silicon surface. From the very flat depth distribution of simulations at 50 eV and 45° incidence angle, we can conclude that the proportion of atoms effectively entering the channels versus those not entering is about 50/50, which sets the window on an azimuth plane to enter the channel to about 45°. This is supported by experimental results reported in [39] where both maxima in

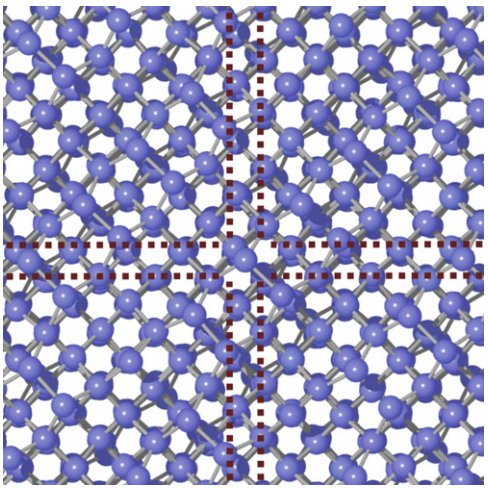

Figure 8. ⟨100⟩ top view representation of the directions followed by the (101) and (011) channels inside the silicon structure.

the intensities of the depth profiles in the (110) direction have equal intensities.

Let us now take time to analyse deeper the reason for the different depth distributions at 50 eV–60° observed with Kieffer and Erhart–Albe potentials. It is known from figure 3 that energies and forces between carbon and silicon increase faster at higher energies for the Erhart–Albe than for the Kieffer potential. These steeper forces mean that it is easier for the carbon atom to enter the channel when outside the correct azimuth window, effectively widening it. With the weaker repulsive forces of the Kieffer potential, the carbon is more likely to form bonds with silicon atoms before being deviated into the channels. This effect can also be observed, albeit to a lesser extent, for deposition at 30°. At 0° no differences between the potentials can be observed because the channel is completely out of reach for the carbon atom. This explains the stronger stopping power at shallow depth for incoming directions slightly out of the perfect channel window, i.e. 45°.

5.2.3. Comparison with DFT. DFT calculations for carbon adsorption have been performed on different sites on and underneath the surface plane. On the surface, two adsorption sites have been identified with very similar adsorption energies of 7.26 and 7.16 eV. The most stable geometry is when carbon adsorbs *vis-á-vis* of a surface silicon dimer, creating bonds with three silicon atoms (figure 9(a)). The three Si–C bond lengths are 1.76, 1.90 and 1.90 Å. On the side of the silicon dimer where the carbon adsorbs, the dimer is now only linked to the material through the carbon atom, breaking two Si–Si bonds at the benefit of three Si–C bonds. The other adsorption site (figure 9(b)) is located in between two silicon dimers. The distortion of the silicon surface is lower, but the carbon atom is only bonded with two silicon atoms (1.82 Å both), explaining the slightly lower adsorption energy. In parallel to these two surface adsorption sites, we have identified two other sites for carbon deposition under the surface plane (figures 9(c) and (d)) with adsorption energies of 7.87 and 8.10 eV, which are significantly more stable than those on the surface plane. In both subsurface sites, the carbon atom sits tetrahedrally bonded beneath a surface silicon dimer. In the most stable configuration (figure 9(d)), there is a strong distortion of the silicon structure around the carbon defect, with a silicon atom now protruding on the surface between two silicon dimers. The four Si–C bond lengths are 1.82, 1.82, 1.92, and 2.04 Å. On the other subsurface site (figure 9(c)), no silicon atom is pushed out of its initial location. Its higher energy shows that the distortion observed in figure 9(d) allows the structure to decrease the internal stress induced by the interstitial carbon atom. These DFT results show a qualitative agreement with the MD simulations presented above, as both methods show that carbon atoms tend to favour subsurface deposition sites. Indeed figure 5 shows that, provided it has enough energy to pass through the first layer of the surface, the

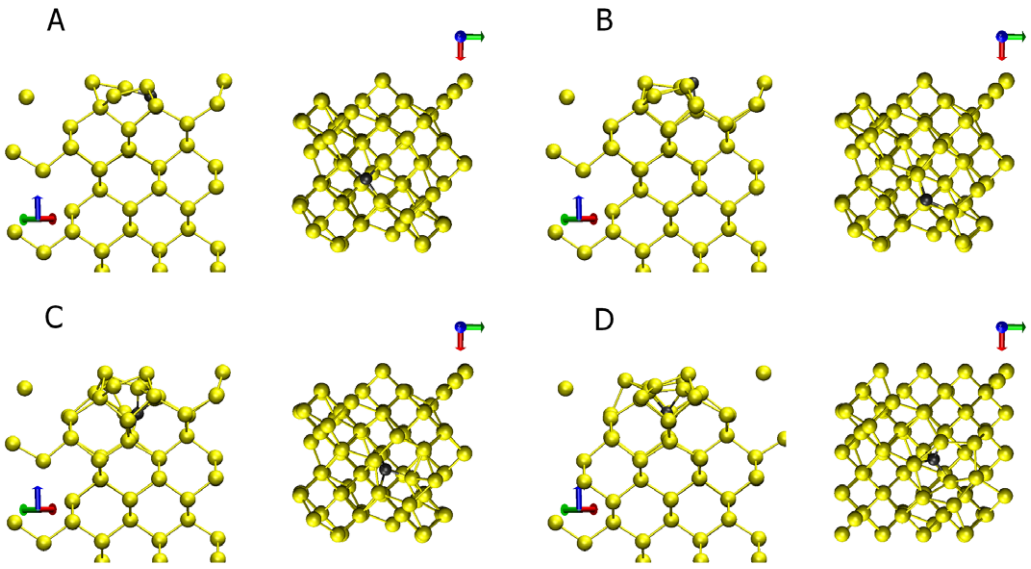

Figure 9. Top and side views of four adsorption sites for carbon on the (100) surface as computed by DFT.

carbon deposit is more likely to stay 2.5 Å below the surface plane.

5.2.4. Sticking coefficient. Due to the shortness of our simulations, 6 ps for the Kieffer potential and 5 ps for the Erhart–Albe potential, the sticking coefficient of carbon on silicon is not directly achievable from the backscattering yields presented earlier. Some deposited matter may eventually desorb from the collector by simple thermal activation, leading to a lower sticking coefficient than the one measured within the first 6 ps of the deposition. This loss of matter by thermal activation is not easy to quantify as, ideally, one would need to perform kinetic Monte Carlo simulations knowing the activation energy for carbon desorption from different deposition sites as well as the activation energies for surface diffusion, coalescence, etc [9]. An easier way, albeit still computationally expensive, to assess this loss due to thermal activation is to let the MD simulations run for significantly longer times. Two deposition conditions using the Kieffer potential are selected to run the extra MD simulations for significantly longer timing using the last configuration of their corresponding simulation as starting point. The first condition is the one with deposition at 50 eV–60° in order to have a highly energetic system and a relatively shallow deposit. The second run has deposition conditions of 1 eV–0° to have a high load of carbon deposit at very shallow depths. Simulations are run using a 1 fs time step for 200 ps. No desorption of carbon from the collector due to thermal activation could be observed within the 200 ps of the simulations. This leads us to conclude that the thermal desorption of carbon from the silicon wafer is very low and the backscattering yields observed in figure 4 may be a reasonable first approximation to assess the sticking coefficients, as they are the inverse of the backscattering yields. Deposition incidence angle close to the normal gives rather high sticking coefficients. Depending on the initial energy of the carbon atom, the sticking coefficients range from 100 to 92%, 100 to 95%, 100 to 93%, 100 to 90% for 0°, 15°, 30°, 45° and 60° incidence angles respectively. At the most grazing incidence angle, the sticking coefficient drops significantly as it ranges within 100–73%.

6. Conclusion and outlook

With the view of performing analyses of alloys materials using the storing matter technique developed at the Centre de Recherche Public—Gabriel Lippmann in Luxembourg, we present the first steps of a MD investigation of carbon deposition on silicon surfaces. The reactive force field developed by Kieffer is selected, as it enables the formation and breaking of bonds via an adaptive and environment sensitive charge transfer. As only parameters describing Si–Si interactions are available in the literature, new sets of parameters for Si–C and C–C are developed using an in-house genetic algorithm. The Si–C and C–C parameter sets are tested and validated on their abilities to model physical properties as well as formation energies of point defects of silicon carbide and diamond. The performances of the force field are in line with other previously published force fields.

In a second step, the deposition of a single carbon atom on a (100) reconstructed silicon surface at energies lower than 50 eV is investigated and compared to similar MD simulations performed using the well-established Erhart–Albe potential. 100 independent simulations are run in order to have significant statistics. Results using both potentials are similar, although slight divergences appear at grazing angles and for the higher end of the deposition energies. These small differences are attributed to the very different approaches used by the two force fields, as the Erhart–Albe potential is a Tersoff-like bond order potential. Nevertheless, the overall agreement between the two potentials for carbon deposition coupled with the performance of the Kieffer potential to model physical properties of silicon carbide and diamond allow us to validate the Kieffer potential for the study of low-energy carbon deposition on silicon surfaces.

The carbon deposition investigations also revealed a channelling effect when implanting carbon at angles close to 45°. The channels are also open, albeit to a lesser extent, to deposition trajectories at 30° and 60° relative to the surface normal. This channelling effect is due to channels running through the silicon crystalline structure at directions symmetrically equivalent to the (110) direction. Therefore, on an azimuthal plane, four orthonormal channels are available from the (100) surface. The azimuthal window for a carbon to enter these channels is estimated at 45°.

Although the MD simulations are run over a rather short timescale, the sticking coefficients of carbon on pristine (100) silicon can be estimated. As expected, the sticking coefficients are lowest at grazing angles and range from 100% to 73% at 60°. Other angles lead to sticking coefficients higher than 90%.

As next steps for the investigation of carbon deposition on silicon surfaces, it will be interesting to focus on amorphous surfaces and on rough surfaces, in order to check how the morphology of the silicon surface will influence the deposition. Also, the continuous deposition of carbon on silicon will be considered, in order to simulate systems closer to the experiments.

Acknowledgments

The present project is supported by the National Research Fund, Luxembourg (C09/MS/15) and co-funded by the Marie Curie Actions of the European Commission (FP7-COFUND). KN and LM acknowledge grants of computer time from the Center for Scientific Computing in Espoo, Finland, and funding from the Academy of Finland—MATERA+ project DESTIMP. The authors wish to thank Professor John Kieffer for his help and advice on this work.

References

[1] Graves D B and Brault P 2009 *J. Phys. D: Appl. Phys.* **42** 191011
[2] Wirtz T and Migeon H N 2008 *Appl. Surf. Sci.* **255** 1498–500

[3] Wirtz T, Mansilla C, Verdeil C and Migeon H N 2009 *Nucl. Instrum. Methods* B **267** 2586–8
[4] Becker N, Wirtz T and Migeon H N 2011 *Surf. Interface Anal.* **43** 413–6
[5] Mansilla C and Wirtz T 2010 *J. Vac. Sci. Technol.* B **28** C1C71–6
[6] Robinson M T and Torrens I M 1974 *Phys. Rev.* B **9** 5008–24
[7] Hobler G and Betz G 2001 *Nucl. Instrum. Methods* B **180** 203–8
[8] Nordlund K 2002 *Nucl. Instrum. Methods* B **188** 41–8
[9] Lucas S and Moskovkin P 2010 *Thin Solids Films* **518** 5355–61
[10] Ziegler J F, Biersack J P and Littmark U 1985 *The Stopping and Range of Ions in Matter* (New York: Pergamon)
[11] Belko V, Posselt M and Chagarov E 2003 *Nucl. Instrum. Methods* B **202** 18–23
[12] Shapiro M H and Lu P 2004 *Nucl. Instrum. Methods* B **215** 326–36
[13] Huang L P and Kieffer J 2003 *J. Chem. Phys.* **118** 1487–98
[14] Huang L P and Kieffer J 2006 *Phys. Rev.* B **74** 224107
[15] Huang L P and Kieffer J 2006 *Nature Mater.* **5** 977–81
[16] Philipp P, Briquet L, Witrz T and Kieffer J 2011 *Nucl. Instrum. Methods* B **269** 1555–8
[17] Angibaud L, Briquet L, Philipp P, Wirtz T and Kieffer J 2011 *Nucl. Instrum. Methods* B **269** 1559–63
[18] Erhart P and Albe K 2005 *Phys. Rev.* B **71** 035211
[19] Tersoff J 1990 *Phys. Rev. Lett.* **64** 1757–60
[20] Soler J M, Artacho E, Gale J D, García A, Junquera J, Ordejón P and Sánchez-Portal D 2002 *J. Phys.: Condens. Matter.* **14** 2745–79
[21] Perdew J P, Burke K and Ernzerhof M 1996 *Phys. Rev. Lett.* **77** 3865–8
[22] Troullier N and Martins J L 1991 *Phys. Rev.* B **43** 1993–2006
[23] Junquera J, Paz Ó, Sánchez-Portal D and Artacho E 2001 *Phys. Rev.* B **64** 235111
[24] Herrero C P and Ramirez R 2000 *Phys. Rev.* B **63** 024103
[25] Wu B R and Xu J 1998 *Phys. Rev.* B **57** 13355
[26] Grimsditch M H and Ramdas A K 1975 *Phys. Rev.* B **11** 3139–48
[27] Bosak A and Krisch M 2005 *Phys. Rev.* B **72** 224305
[28] Patnaik P 2003 *Handbook for Inorganic Chemicals* (New York: McGraw-Hill)
[29] Lambrecht W R L, Segal B, Methfessel M and van Schilfgaarde M 1991 *Phys. Rev.* B **44** 3685–94
[30] Gao F and Weber W J 2002 *Nucl. Instrum. Methods* B **191** 504–8
[31] Bağci S, Duman S, Tütüncü H M and Srivastava G P 2009 *Diamond Relat. Mater.* **18** 1057–60
[32] Bernholc J, Antonelli A, Del Sole T M, Bar-Yam Y and Panteledis S T 1988 *Phys. Rev. Lett.* **61** 2689–92
[33] Shim J, Lee E K, Lee Y J and Nieminem R M 2005 *Phys. Rev.* B **71** 035206
[34] Gao F, Bylaska E J, Weber W J and Corrales L R 2001 *Phys. Rev.* B **64** 245208
[35] Nord J, Albe K, Erhart P and Nordlund K 2003 *J. Phys.: Condens. Matter* **15** 5649
[36] Berendsen H J C, Postma J P M, van Gunsteren W F, DiNola A and Haak J R 1984 *J. Chem. Phys.* **81** 3684–90
[37] Samela J and Nordlund K 2007 *Nucl. Instrum. Methods. Phys. Res.* B **263** 375–88
[38] Nordlund K 1995 *Comput. Mater. Sci.* **3** 448–56
[39] Raineri V, Privitera V, Galvagno G, Priolo F and Rimini E 1994 *Mater. Chem. Phys.* **38** 105–30